Sensorless SVPWM-FADTC of a New Flux-Modulated Permanent-Magnet Wheel Motor Based on a Wide-Speed Sliding Mode Observer

Ying Fan, *Senior Member, IEEE*, Li Zhang, *Student Member, IEEE*, Ming Cheng, *Fellow, IEEE*, and K. T. Chau, *Fellow, IEEE*

***Abstract*—This paper presents a sensorless flux adaption-direct torque control (FADTC) for a new flux-modulated permanent-magnet (FMPM) wheel motor, in which space-vector pulsewidth modulation (SVPWM) and a wide-speed sliding mode observer (SMO) are adopted. SVPWM-FADTC has several advantages over conventional hysteresis direct torque control, such as low torque/flux ripples in motor drive and reduced direct axis current when the motor is operated at a light or a sudden increased load. To achieve the sensorless control of SVPWM-FADTC system, a wide-speed SMO is proposed. Compared with conventional SMO, system chattering is improved, the low-pass filter and the phase compensation are eliminated, and the estimation accuracy of the rotor position at low speed is enhanced. Numerical simulations and experiments with a 2-kW FMPM wheel motor are carried out. The results verify the feasibility and effectiveness of the proposed sensorless SVPWM-FADTC method adopted by the FMPM wheel motor.**

***Index Terms*—Direct torque control (DTC), flux-modulated wheel motor, permanent-magnet (PM) motor, sliding mode observer (SMO).**

I. Introduction

DUE to the advantages of simple structure and high efficiency, the permanent-magnet (PM) wheel motor is widely used in electric vehicles (EVs). A PM wheel motor drive has two types: One is low-speed gearless outer-rotor drive, and another is high-speed planetary-geared inner-rotor drive. The former has the drawbacks of bulky size and heavy weight because of its low speed, and the latter has the disadvantages of transmission loss, regular lubrication, and acoustic noise because of its mechanical planetary gear. Magnetic gear has been paid much attention in recent years since it can provide overload protection, high reliability and efficiency, reduced acoustic noise, and no maintenance [1, 2]. A magnetic-geared PM wheel motor has been proposed in [3]; it artfully integrates a magnetic gear into a PM brushless dc motor so that they can share a common PM rotor, hence offering high efficiency and high torque density. Moreover, the low-speed requirement for direct driving and the high-speed requirement for compact motor design can be achieved simultaneously. However, it has a complicated structure with three air gaps, which results in high costs and complex manufacture. Hence, in this paper, a new flux-modulated PM (FMPM) wheel motor is proposed. Due to the omitted inner rotor and stationary ring, there is only one air gap between a stator and an outer rotor. Therefore, the structure is highly simplified, and the torque density is greatly enhanced. Moreover, the merits such as direct drive, low speed, and large torque output make this FMPM wheel motor a promising candidate for driving EVs.

Direct torque control (DTC) has the advantages of rapid torque response, simple structure, and less parameter dependence [4, 5]. Due to these characteristics, it can meet the high performance requirement for EVs. Nevertheless, conventional hysteresis DTC presents some drawbacks such as large torque ripple and variable switching frequency [6]. Instead, DTC based on space-vector modulation (SVM-DTC) can obtain fixed switching frequency and lower torque ripple [7, 8]. In the DTC system, to control its torque by controlling the torque angle, the stator flux amplitude is constant. Thus, when the motor runs at a light or a sudden increased load, the d-axis current is increased to maintain the stator flux a constant, which will increase the loss of the motor and reduce its efficiency [9, 10]. To solve this problem, a strategy of stator flux linkage control based on maximum torque per ampere is proposed and implemented for interior PM synchronous motors [10]. However, this algorithm is relatively complex due to the solution of the nonlinear equations. In [9], a novel DTC scheme of "$i_d = 0$" is proposed. It is simple and greatly improves the efficiency. Nevertheless, the shortcomings of conventional hysteresis DTC have not been overcome. In this paper, a flux adaption-DTC based on space-vector pulsewidth modulation (SVPWM-FADTC) is proposed.

To achieve precise torque control of the new FMPM wheel motor in the DTC system, an accurate rotor position is needed. The electromechanical position sensors are commonly used to obtain the rotor position. However, the use of these sensors causes a series of problems such as additional cost, reduction of reliability, and complexity of the drive system [11]. To

Manuscript received April 28, 2014; revised July 21, 2014 and September 23, 2014; accepted October 17, 2014. Date of publication December 4, 2014; date of current version April 8, 2015. This work was supported in part by the National Natural Science Foundation of China under Project 51177012 and Project 61374125 and in part by the 973 Program of China under Project 2013CB035603.

Y. Fan, L. Zhang, and M. Cheng are with the School of Electrical Engineering, Southeast University, Nanjing 210096, China (e-mail: vickifan@seu.edu.cn; zhangli_870816@163.com; mcheng@seu.edu.cn).

K. T. Chau is with the Department of Electrical and Electronic Engineering, The University of Hong Kong, Pokfulam, Hong Kong (e-mail: ktchau@eee.hku.hk).

Color versions of one or more of the figures in this paper are available online at http://ieeexplore.ieee.org.

Digital Object Identifier 10.1109/TIE.2014.2376879

overcome these drawbacks, sensorless control has been paid much attention. Currently, according to the different applicable speed ranges, sensorless control algorithms can be categorized into two main approaches: One is a high-frequency injection method, and another is a back electromotive force (EMF) estimation method. Due to the salient effect, the former is independent on motor parameters and has an accurate estimation at zero/low speed [12, 13]. Nevertheless, high-frequency noise brought by high-frequency injection signal will deteriorate the system performance. The latter is suitable for salient and nonsalient motors and exhibits good dynamic and static performance at medium/high speed [14, 15]. However, the low-speed estimated performance is relatively poor. Owing to the low saliency of the new FMPM wheel motor, the latter is more appropriate than the former.

Among several kinds of sensorless control algorithms, the sliding mode observer (SMO) is especially attractive for sensorless control of the new FMPM wheel motor because of the distinctive advantages of high reliability and good robustness to large load variations. However, chattering caused by discontinuous switching is an inevitable problem in the SMO [16, 17]. Therefore, the key of SMO is to minimize chattering and improve the low-speed estimated accuracy. In [18], the sigmoid function is used instead of the conventional switching function to significantly reduce system chattering. However, the use of a low-pass filter (LPF) results in a phase delay problem; thus, the estimated accuracy is reduced. In [19], the phase delay problem caused by LPF is solved, but the analysis of low-speed estimated performance is ignored. In [20], an adaptive algorithm of the back EMF gain is proposed to enhance low-speed estimated accuracy, but the phase compensation is still required, which makes the estimated accuracy of the whole drive system worse. Therefore, it is necessary to develop a wide-speed SMO method for the sensorless control.

The major contribution of this paper is to propose a sensorless SVPWM-FADTC method for the new FMPM wheel motor to obtain the following performances: low torque ripples, reduced d-axis current at a light or sudden increased load, and a good estimated performance in a wide operating range. This paper is organized as follows. In Section II, the operating principle and characteristics of the new FMPM wheel motor are described. The SVPWM-FADTC scheme of this motor is analyzed in Section III. In Section IV, descriptions of the wide-speed SMO and sensorless DTC system of this FMPM wheel motor are presented in detail. Simulation and experimental results are analyzed in Section V. Finally, conclusions are stated in Section VI.

II. Motor Description

A. Operating Principle

The proposed FMPM wheel motor is shown in Fig. 1. It can be noted that there is only one air gap between a stator and an outer rotor of the proposed motor. The stator core has slots of total number z_s, in which three phase windings with pole pairs p_s are wound. On the other hand, slots of total number of p_r are punched at equal distance along the periphery of the

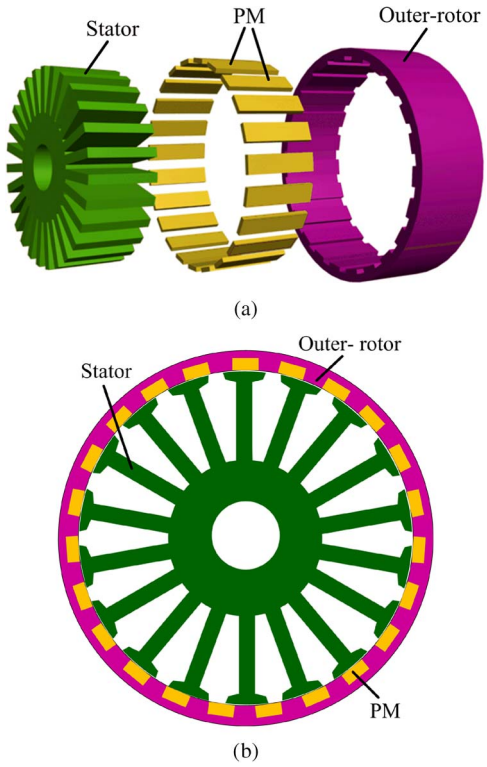

Fig. 1. Configuration of the proposed FMPM wheel motor. (a) Three-dimensional view. (b) Sectional view.

rotor core. Its operating principle is similar with the PM vernier machine in [21], which is based on the rule called the "magnetic gearing effect". That is, a small movement of the rotor makes a large change of the flux, which results in high torque. In this proposed FMPM wheel motor, the stator teeth are designed to modulate the high-speed rotating field of the three phase stator windings to the low-speed rotating field of the PM outer rotor. Thus, self-decelerating operation is realized, and high-torque output is achieved.

Similar with the magnetic-geared PM brushless motor in [22] or the flux-controllable vernier PM machine in [23], to maximize the useful fundamental harmonic field and produce steady torque [2], this motor should satisfy

$$z_s = p_s + p_r. \tag{1}$$

Hence, the high-to-low speed ratio G_r is expressed as

$$G_r = -\frac{P_r}{P_s} \tag{2}$$

where the "−" means that the fundamental magnetic field of the armature winding is in the opposite direction of rotation of the outer rotor. In these parameters, z_s is chosen to be multiples of three to realize three-phase topology. To minimize the torque ripple and perform torque transmission, p_r and p_s are designed as 23 and 4, respectively. Then, according to (1), z_s is 27. From (2), it yields $G_r = 5.75$. It means that the outer rotor speed is only 4/23 of that in stator for armature rotating field speed. Thus, when the speed of the rotating field in the stator is 2300 r/min, the speed of the outer rotor is 400 r/min approximately. It can satisfy the requirements of wheel motor in EVs.

TABLE I
PARAMETERS OF THE FMPM WHEEL MOTOR

Parameters	Units	Values
Rated voltage U_N	V	130
Rated power P	kW	2
Rated speed of outer rotor n_N	r/min	400
Rotational inertia J	kg·m^2	0.06
Flux linkage of PM ψ_f	Wb	0.1368
Stator resistance R_s	Ω	0.77
Stator inductance L_s	mH	11.9
Outer rotor PM pole-pairs		23
Torque	N·m	48
Torque density	N·m/L	36.4

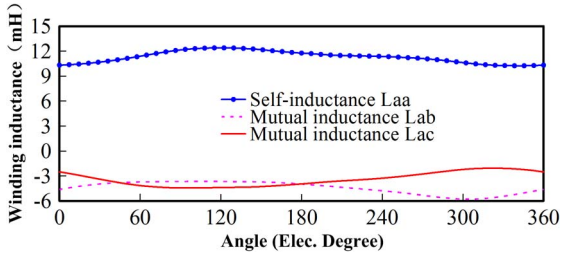

Fig. 2. Winding inductance of phase A.

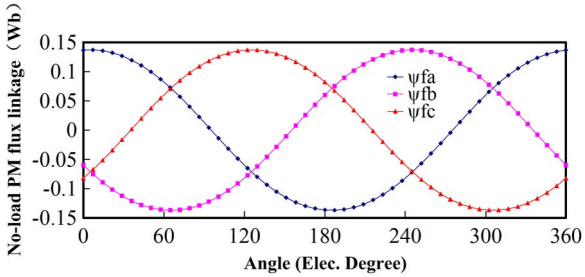

Fig. 3. No-load PM flux of three phases.

B. Motor Characteristics

The parameters of the FMPM wheel motor are listed in Table I. Based on the finite-element analysis of the FMPM wheel motor, the static characteristics are analyzed. Fig. 2 shows the winding inductances of phase A. It is shown that self-inductance and mutual inductance of phase A are approximately consistent. The no-load PM flux linkages of three phases are sinusoidal, as shown in Fig. 3. It indicates that the back EMF waveforms of stator winding are sinusoidal. Therefore, the new FMPM wheel motor is more suitable for sinusoidal current drive.

III. SVPWM-FADTC SCHEME OF THE NEW FMPM WHEEL MOTOR

As it has been demonstrated in [8], the SVM-DTC scheme based on expected voltage vector modulation is implemented well. However, when the new FMPM wheel motor is operated at a light load or a sudden increased load, the required torque is very small [9], [24]. Hence, the additional d-axis current component is required to maintain the stator flux a constant. The d-axis current does not produce torque, and the reactive power component of stator current increases. Thus, with the increased value of the d-axis current, loss of the FMPM motor will be increased and its efficiency will be decreased. To reduce the d-axis current in DTC, a flux linkage adaptive approach [24] is investigated in this paper.

The flux linkages and the electromagnetic torque in dq frame are shown as follows:

$$\begin{cases} \Psi_d = L_s i_d + \Psi_f \\ \Psi_q = L_s i_q \end{cases} \tag{3}$$

$$T_e = \frac{3}{2} P_r \Psi_f i_q \tag{4}$$

where L_s is the phase inductance; $i_{d,q}$ and $\Psi_{d,q}$ represent the phase currents and flux linkages in dq frame, respectively; ψ_f is the PM flux linkage; and T_e is the electromagnetic torque.

In (3), setting $i_d = 0$ and combined with (4), the stator flux reference can be deduced as

$$\begin{cases} \psi_d^* = \psi_f \\ \psi_q^* = \frac{2T_e L_s}{3P_r \psi_f} \\ \psi^* = \sqrt{\psi_d^{*2} + \psi_q^{*2}} \end{cases} \tag{5}$$

where ψ^* is the stator flux reference, and $\psi_{d,q}^*$ represent the stator flux references in dq frame.

Therefore, the reference stator flux linkage is not a constant, and it changes with the load torque.

The proposed SVPWM-FADTC scheme is shown in Fig. 4. The flux linkage adaption is used to obtain the reference stator flux linkage amplitude. The reference stator flux linkage vector is determined by the reference angular frequency of the stator flux linkage (the output of the PI torque regulator) and the reference flux linkage position. Then, the expected voltage vectors and their duration are chosen and calculated by the flux linkage vector error; hence, the error can be reduced to zero.

The SVPWM-FADTC scheme of the new FMPM wheel motor shown in Fig. 4 exhibits many advantages. Because the SVPWM technique is adopted instead of the switching table in conventional DTC, the torque/flux ripples are decreased, the switching frequency is fixed, and the current waveforms are significantly improved accordingly. Moreover, due to the utilization of the flux linkage adaptive approach, the d-axis current component is greatly reduced, and efficiency of the motor can be enhanced correspondingly.

IV. SENSORLESS CONTROL BASED ON WIDE-SPEED SMO

Due to the use of sign function as the sliding mode variable structure function, conventional SMO suffers from chattering. The LPF is needed to eliminate the chattering from the switching, and it will lead to the phase delay, and then an extra compensation is required to estimate the rotor position. Moreover, the poor performance of low-speed estimation makes the operation range narrowed. Therefore, a wide-speed SMO is proposed in this paper.

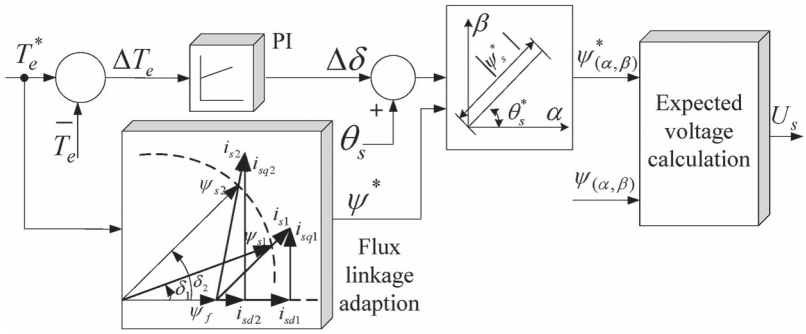

Fig. 4. Block diagram of the SVPWM-FADTC scheme.

A. Design of the Back EMF Observer

The back EMF equations of the new FMPM wheel motor in $\alpha\beta$ frame are

$$\begin{cases} e_\alpha = -\psi_f \omega_e \sin\theta \\ e_\beta = \psi_f \omega_e \cos\theta \end{cases} \tag{6}$$

where $e_{\alpha,\beta}$ are the back EMFs in $\alpha\beta$ frame; ω_e is the electrical angular velocity; and θ is the rotor position with electric degree.

Based on [17], the back EMF observer can be constructed and the asymptotical stability is verified.

The equations of the back EMF observer are given as follows:

$$\begin{cases} \frac{d\hat{e}_\alpha}{dt} = -\hat{\omega}_e \hat{e}_\beta - l_1(\hat{e}_\alpha - e_\alpha) \\ \frac{d\hat{e}_\beta}{dt} = \hat{\omega}_e \hat{e}_\alpha - l_1(\hat{e}_\beta - e_\beta) \\ \frac{d\hat{w}_e}{dt} = (\hat{e}_\alpha - e_\alpha)\hat{e}_\beta - (\hat{e}_\beta - e_\beta)\hat{e}_\alpha \end{cases} \tag{7}$$

where $\hat{e}_{\alpha,\beta}$ are the estimated back EMFs in $\alpha\beta$ frame; $\hat{\omega}_e$ is the estimated electrical angular velocity; and l_1 represents the observer gain, which is greater than zero.

B. Design of the Wide-Speed SMO Observer

The voltage equations of the FMPM wheel motor in $\alpha\beta$ frame can be expressed as

$$\begin{cases} \frac{di_\alpha}{dt} = -\frac{R_s}{L_s} i_\alpha - \frac{1}{L_s} e_\alpha + \frac{1}{L_s} u_\alpha \\ \frac{di_\beta}{dt} = -\frac{R_s}{L_s} i_\beta - \frac{1}{L_s} e_\beta + \frac{1}{L_s} u_\beta \end{cases} \tag{8}$$

where $i_{\alpha,\beta}$ and $u_{\alpha,\beta}$ are the stator currents and the stator voltages in $\alpha\beta$ frame, and R_s is the stator resistance.

Based on the idea of sliding mode in [25] and by using sigmoid function as the sliding mode variable structure function, then (8) can be rewritten as

$$\begin{cases} \frac{d\hat{i}_\alpha}{dt} = -\frac{R_s}{L_s} \hat{i}_\alpha - \frac{1}{L_s}(u_\alpha - l_2 H_{e\alpha} - H_\alpha) \\ \frac{d\hat{i}_\beta}{dt} = -\frac{R_s}{L_s} \hat{i}_\beta - \frac{1}{L_s}(u_\beta - l_2 H_{e\beta} - H_\beta) \end{cases} \tag{9}$$

where $\hat{i}_{\alpha,\beta}$ are the estimated currents in the $\alpha\beta$-axis; H is the sigmoid function that replaces the conventional switching function; $H_{\alpha,\beta}$ is H in $\alpha\beta$ frame; H_e is the equivalent control function, which is obtained by back EMF observer from H; $H_{e\alpha,\beta}$ is H_e in $\alpha\beta$ frame; and l_2 is the feedback gain coefficient of H_e.

The variable structure system is defined as

$$H = \begin{bmatrix} H_\alpha \\ H_\beta \end{bmatrix} = k \times \text{sigmoid}(S) = k\left[\frac{2}{1+e^{-ax}} - 1\right] \tag{10}$$

where a is the adjustable parameter, k is the switching gain of H, and $S = \hat{i} - i$ is the current error between the estimated current and the actual current.

By subtracting (8) from (9), the dynamic equation of the wide-speed SMO can be depicted as

$$\begin{cases} \frac{dS_\alpha}{dt} = -\frac{R_s}{L_s} S_\alpha + \frac{1}{L_s}(e_\alpha - l_2 H_{e\alpha} - H_\alpha) \\ \frac{dS_\beta}{dt} = -\frac{R_s}{L_s} S_\beta + \frac{1}{L_s}(e_\beta - l_2 H_{e\beta} - H_\beta) \end{cases} \tag{11}$$

where $S_{\alpha,\beta}$ are the current errors in $\alpha\beta$ frame.

Once the system slides on a sliding mode surface, then the sliding surface becomes as follows:

$$\begin{cases} S_\alpha = \hat{i}_\alpha - i_\alpha = 0 \\ S_\beta = \hat{i}_\beta - i_\beta = 0. \end{cases} \tag{12}$$

Substituting (12) into (11), one obtains

$$\begin{cases} e_\alpha = H_\alpha + l_2 H_{e\alpha} \\ e_\beta = H_\beta + l_2 H_{e\beta}. \end{cases} \tag{13}$$

Furthermore, back EMF from (13) can be used to calculate the rotor approximate electric angle $\hat{\theta}$ as follows:

$$\hat{\theta} = -\tan^{-1}\left(\frac{e_\alpha}{e_\beta}\right) = -\tan^{-1}\left(\frac{H_{e\alpha}}{H_{e\beta}}\right). \tag{14}$$

According to the SMO theory, its stability condition is $S_\alpha^T \dot{S}_\alpha < 0$, $S_\beta^T \dot{S}_\beta < 0$, and then the following can be obtained:

$$S_{\alpha,\beta}^T \times \dot{S}_{\alpha,\beta} = \frac{1}{L_s} S_{\alpha,\beta}(e_{\alpha,\beta} - l_2 H_{e\alpha,\beta} - H_{\alpha,\beta}) - \frac{R_s}{L_s} S_{\alpha,\beta}^2. \tag{15}$$

Due to $-R_s S_\alpha^2 / L_s < 0$, $-R_s S_\beta^2 / L_s < 0$ and combined with (10), the condition that meets for (15) is shown as follows:

$$(1 + l_2)k > \max(|e_\alpha|, |e_\beta|). \tag{16}$$

In (13), it is shown that the magnitude of the equivalent control H_e is always larger than that of the back EMF with the value $-1 < l_2 < 0$. Then, the rotor position can be calculated from H_e instead of the back EMF. Although the back EMF is relatively small at low speed (5%–20% of the rated speed), the estimated H_e is enlarged. Therefore, the wide-speed SMO is

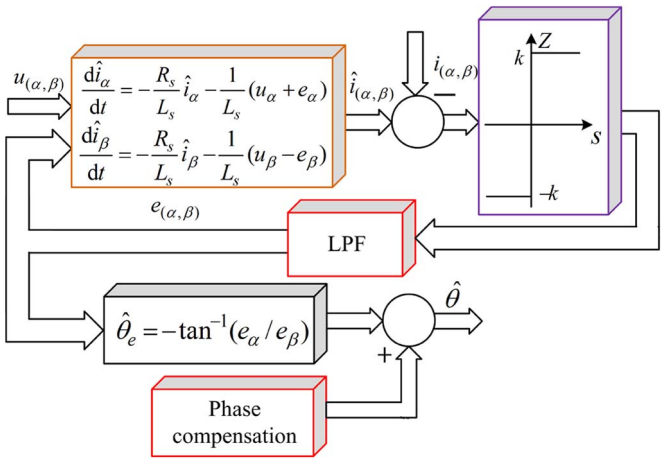

Fig. 5. Block diagram of conventional SMO.

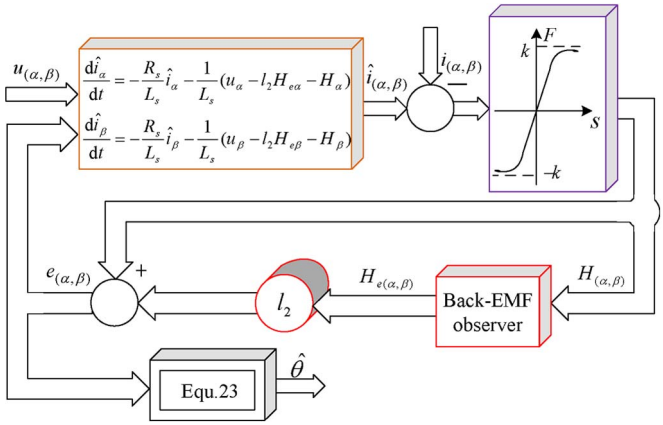

Fig. 6. Block diagram of wide-speed SMO.

able to work at a lower speed and has better position estimated accuracy.

The block diagrams of conventional SMO and wide-speed SMO are shown in Figs. 5 and 6, respectively. In these two figures, it is shown that, in the wide-speed SMO algorithm, the switching function is replaced by the sigmoid function to improve the charting problem of conventional SMO. The back EMF observer is used instead of traditional LPF to achieve the back EMF signal. Furthermore, the adaptive algorithm of the back EMF gain is used to enhance the low-speed estimation accuracy.

For a wheel motor application, reliability of the drive system is very important. The wide-speed SMO algorithm is used to replace the sensor to obtain the rotor position signal in the SVPWM-FADTC drive system; then, the reliability of the DTC system can be enhanced due to the omitted position sensor. The control diagram of the sensorless SVPWM-FADTC of the FMPM wheel motor is shown in Fig. 7.

V. Simulation and Experimental Results

A. Simulation Results

To verify the validity of the sensorless SVPWM-FADTC algorithm adopted by the new FMPM wheel motor, the proposed

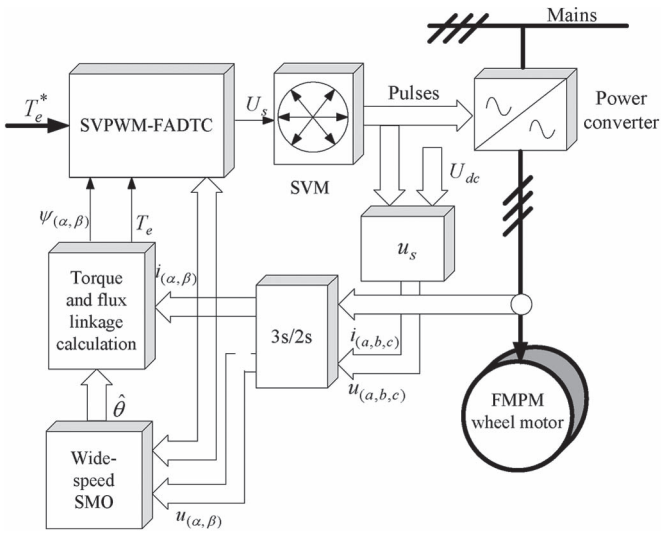

Fig. 7. Simplified block diagram of the proposed sensorless SVPWM-FADTC of the FMPM wheel motor.

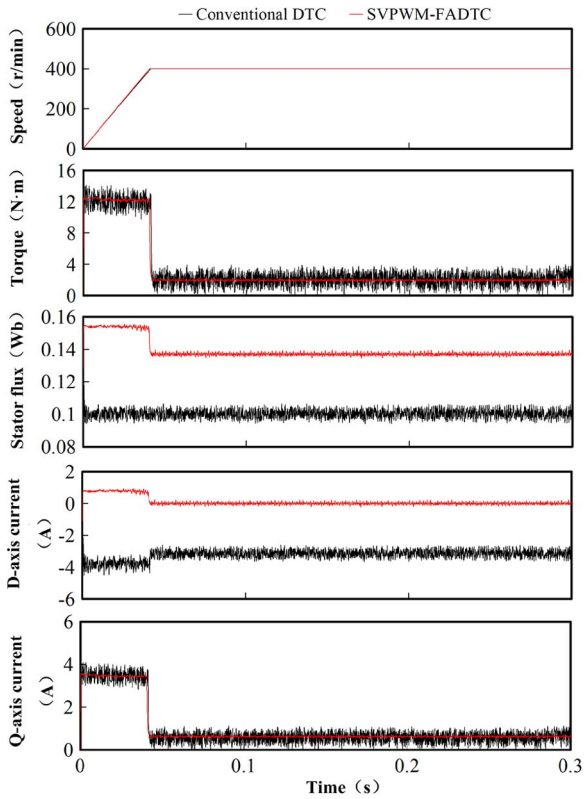

Fig. 8. Simulation waveforms of DTC.

system, as shown in Fig. 7, is simulated by using MATLAB/Simulink.

Fig. 8 shows the simulation results of conventional DTC system and SVPWM-FADTC system with 400 r/min commanded under a light load of 2 N · m, respectively. The waveforms of speed, torque, stator flux amplitude, d-axis current, and q-axis current are included in this figure. It is shown that the torque ripple of conventional DTC is 50%, whereas that of SVPWM-FADTC is 4%, which is reduced greatly and so is the flux ripple. The torque waveforms of both conventional DTC and

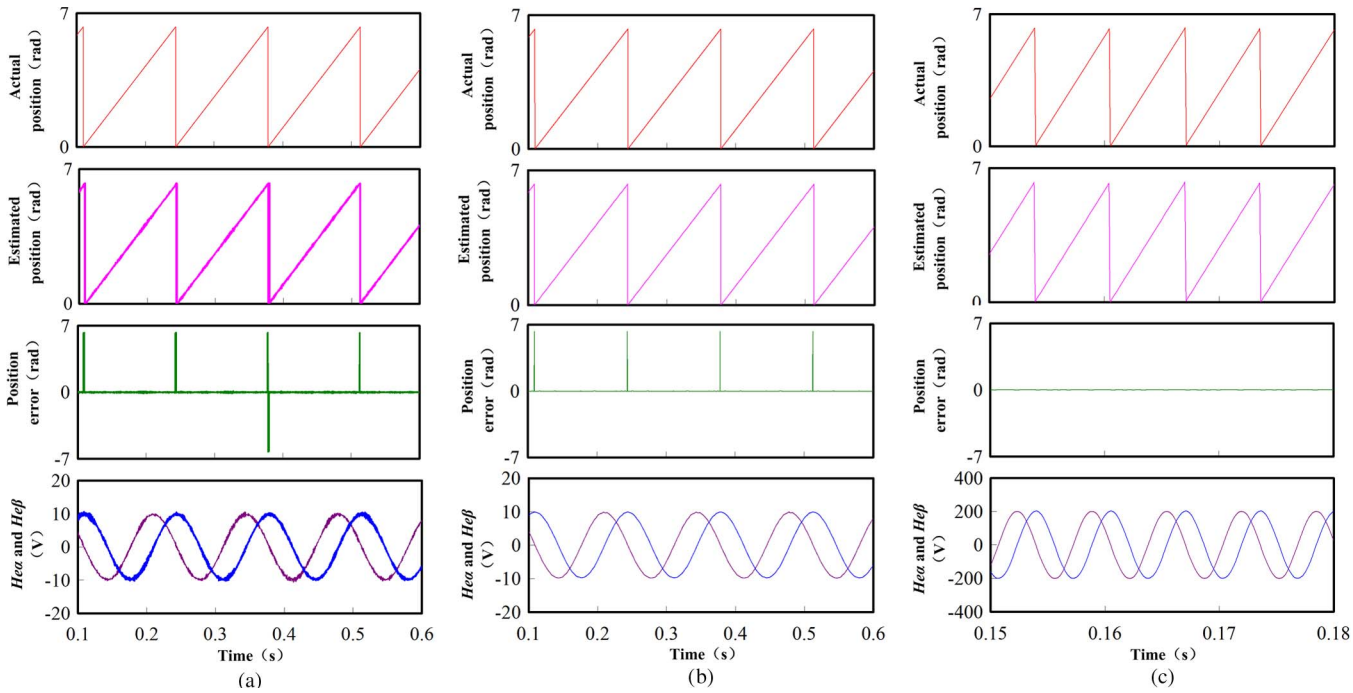

Fig. 9. Simulation waveforms of steady-state performances for sensorless control system. (a) Conventional SMO with 20 r/min commanded. (b) Wide-speed SMO with 20 r/min commanded. (c) Wide-speed SMO with 400 r/min commanded.

SVPWM-FADTC reach reference torque at 0.03 s. Therefore, the advantage of rapid torque response has been retained in the SVPWM-FADTC system. In addition, the d-axis current value of conventional DTC is -3.2 A, whereas that of SVPWM-FADTC is 0.05 A; then, the power factor increases from 18.1% to 99.7% accordingly. The q-axis current is linearly proportional to the torque; hence, the dynamic and steady performance of the q-axis current is the same as that of the torque, and the q-current waveform could reflect the performance of torque. The above analysis demonstrates the effectiveness and advantages of the SVPWM-FADTC algorithm.

To verify the low- and high-speed performances of the wide-speed SMO, Fig. 9 gives the steady-state waveforms obtained by the conventional SMO with 20 r/min commanded, the wide-speed SMO with 20 r/min commanded, and the wide-speed SMO with 400 r/min commanded, respectively. Comparing Fig. 9(a) with Fig. 9(b), it can be noted that there are many performance improvements achieved with the proposed wide-speed SMO: Chattering is reduced when the conventional switching function is replaced by a sigmoid function, the position error is reduced, and the sine of equivalent control function H_e is improved. Hence, the accuracy of position and speed estimation is greatly enhanced, which demonstrates that the wide-speed SMO has a good estimated performance of low speed. With the position error in Fig. 9(c), it can be observed that the proposed sensorless control algorithm has a better tracking capability at high speed. From the above analysis, it can be noted that, based on the wide-speed SMO, whether the motor runs at high speed or low speed, chattering of estimated position and H_e is small and so is the position error. Hence, by using the wide-speed SMO algorithm, the performance of low speed can compete with that of high speed, in which no phase compensation is needed, and has good estimated accuracy.

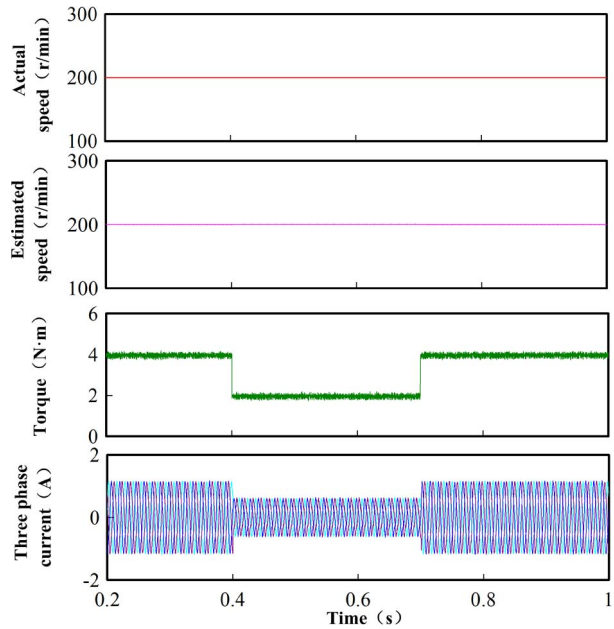

Fig. 10. Dynamic performance of sensorless control based on wide-speed SMO with 200 r/min commanded.

It is very important to maintain a steady and smooth speed during the actual operation for EVs. To verify the performance of the transient responses for the proposed strategy, Fig. 10 shows dynamic performance under a change from load of 4 to 2 $\mathrm{N}\cdot\mathrm{m}$ and then back to 4 $\mathrm{N}\cdot\mathrm{m}$ at reference speed of 200 r/min. It is shown that the dynamic and steady-state performance of the estimated speed waveform is agreed with the actual speed waveform, which fully demonstrates that the system has the performance of a fast response and the capacity of strong robustness.

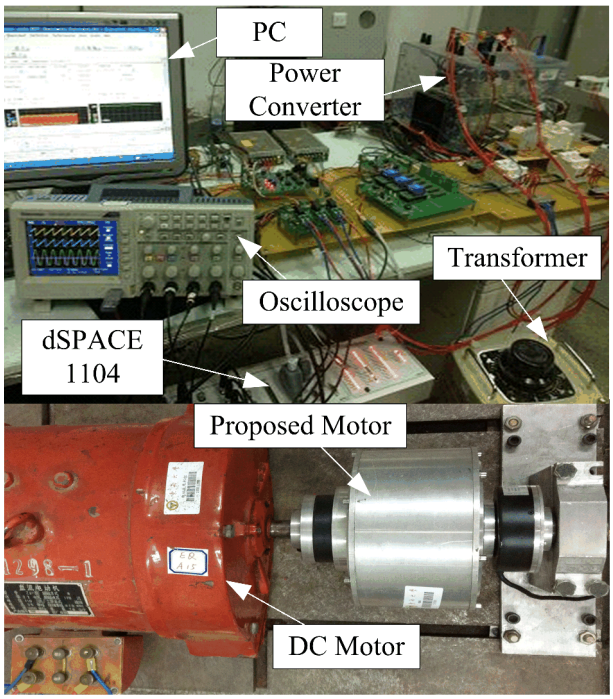

Fig. 11. Experiment platform. (a) Conventional DTC. (b) SVPWM-FADTC.

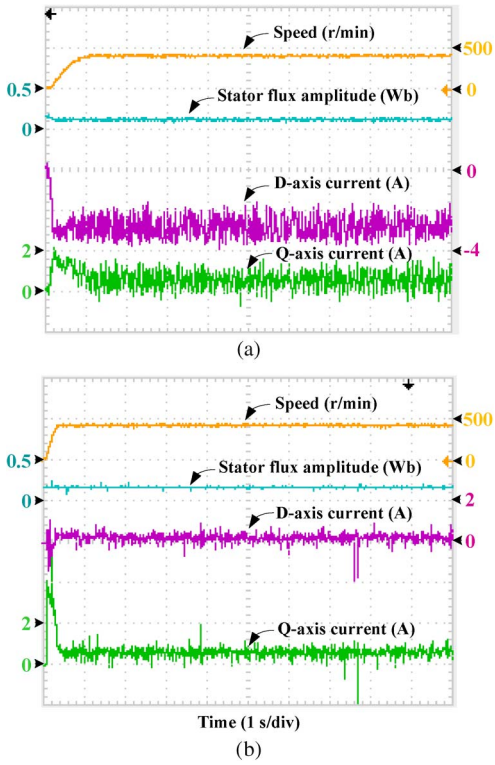

Fig. 12. Experimental waveforms of DTC. (Left) Scale of stator flux amplitude and q-axis current. (Right) Scale of speed and d-axis current.

B. Experimental Results

To further verify the performance of the proposed sensorless SVPWM-FADTC algorithm adopted for the new FMPM wheel motor, a dSPACE 1104 controller is used to drive the prototype. The experiment platform is shown in Fig. 11, which includes the prototype coupled with a 2.2-kW 1500-r/min dc motor as a load, an incremental encoder with 1024 pulses/revolution to obtain the actual rotor position, a three-phase diode bridge rectifier, a voltage source inverter controlled by a dSPACE 1104 controller, and some necessary peripherals.

To verify the validity of the SVPWM-FADTC algorithm, Fig. 12(a) and (b) shows the experimental results of the conventional DTC system and the SVPWM-FADTC system with 400 r/min commanded under a light load of 2 $\mathrm{N}\cdot\mathrm{m}$, respectively. It can be noted that the flux ripples of the SVPWM-FADTC system are greatly reduced compared with that of the conventional DTC system; the torque ripples are accordingly reduced due to the reduced q-axis current ripples. The q-axis current waveform in conventional DTC and SVPWM-FADTC reaches reference value at almost the same time, which illustrates that the advantage of rapid torque response has been retained in the SVPWM-FADTC system. Furthermore, the d-axis current value of conventional DTC is -3 A and that of SVPWM-FADTC is 0.05 A; then, the corresponding power factor of SVPWM-FADTC is largely increased. Comparing the experimental results in Fig. 12 with the simulated results in Fig. 8, it is shown that the experimental d- and q-axis current waveforms have more glitch. This is due to the current sensor in the circuit board, which is influenced by electromagnetic interference.

Fig. 13 displays the experimental steady-state waveforms obtained by the conventional SMO with 20 r/min commanded, the wide-speed SMO with 20 r/min commanded, and the wide-speed SMO with 400 r/min commanded, respectively. In Fig. 13(a) and (b), it is shown that, compared with the conventional SMO, in the wide-speed SMO, the estimated rotor position can better track the actual rotor position since the estimated error is reduced, chattering of estimated rotor position and the equivalent control function H_e is obviously reduced, and the sine of H_e is greatly improved at low speed. Therefore, with the proposed control strategy, the improvement of estimated position and speed at low speed is achieved. As shown in Fig. 13(c), the position error is about zero and the waveform of H_e is ideal sinusoidal at high speed. From the above analysis, it can be concluded that the wide-speed SMO algorithm has an accurate estimation at both high speed and low speed. Comparing the experimental results in Fig. 13 with the simulated results in Fig. 9, it is shown that the amplitude of H_e in the experiment is unequal to that in the simulation. During the adjustment of SMO parameters, such as k and l_2, which are set incompletely identical due to the difference between the experimental hardware system and the simulation software system. This is the reason why the amplitudes of H_e between experiment and simulation are not equal.

From the sensorless control results of the simulation and experiment, it can be observed that the proposed wide-speed SMO can widen the range of speed estimation. However, it still has the problem of zero/lowest speed operation as it is based on back EMF to obtain the position and speed signals. The combination method of high-frequency fluctuating voltage signal injection and wide-speed SMO can solve the aforementioned problem. When the motor is running at less than 20 r/min, the high-frequency fluctuating voltage signal injection method

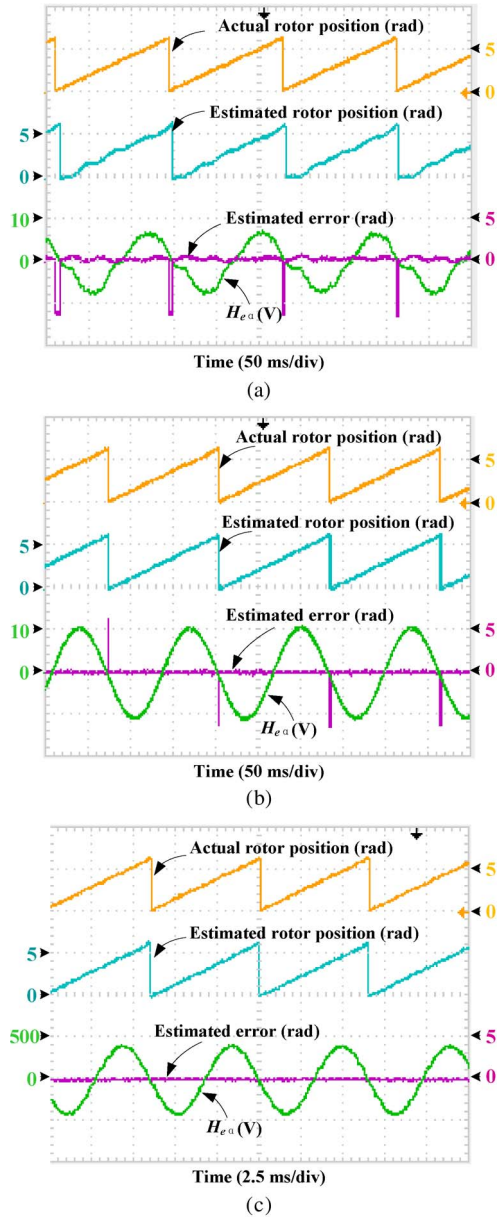

Fig. 13. Experimental waveforms of steady-state performances for sensorless control system. (Left) Scale of estimated rotor position and $H_{e\alpha}$. (Right) Scale of actual rotor position and estimated error.

is used; otherwise, the wide-speed SMO method is applied to ensure dynamic performance and robustness of the driving system. Then, the self-detection of rotor position at full speed range, including zero speed, can be realized, and it will be addressed in the next research.

Fig. 14 shows the transient responses of sensorless control based on the wide-speed SMO under a change from load of 4 to 2 N · m and then back to 4 N · m at 200 r/min. As observed, the rotor actual speed and estimated speed are well regulated regardless of load disturbance. Moreover, two full cycles of the phase current are shown in this figure. With the harmonic analysis, the total harmonic distortion of the phase current is 4.73%, as shown in Fig. 15. It can be obtained that the phase current at full cycle is sinusoidal, although the experimental phase current has some glitch due to the current sensor in the circuit board, which is influenced by electromagnetic interference.

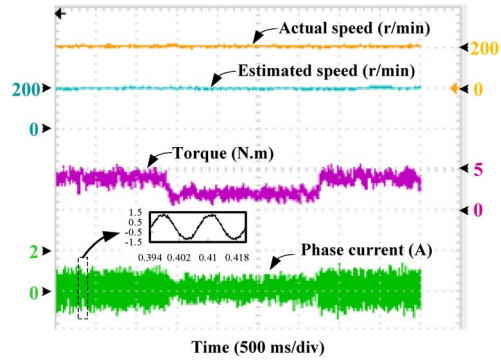

Fig. 14. Performance of sensorless control based on wide-speed SMO with 200 r/min commanded under step load torque. (Left) Scale of estimated speed and phase current. (Right) Scale of actual speed and torque.

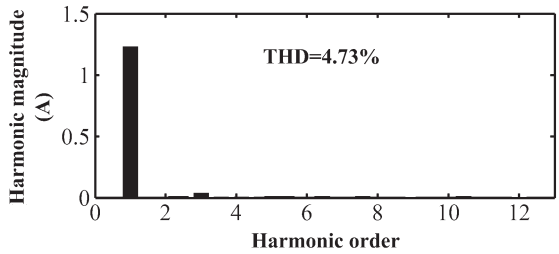

Fig. 15. Harmonic analysis of the steady phase current.

VI. Conclusion

To meet the requirements of high performance for driving system, sensorless SVPWM-FADTC of the new FMPM wheel motor based on wide-speed SMO has been proposed and investigated in this paper. The proposed SVPWM-FADTC algorithm offers advantages of small torque and flux ripples, reduced d-axis current, and enhanced motor efficiency when the motor is operated at a light load or a sudden increased load.

Furthermore, sensorless control based on wide-speed SMO is studied to solve the problems produced by mechanical sensors of the SVPWM-FADTC system; thus, the system reliability is enhanced. Due to the use of the sigmoid function instead of the conventional switching function, system chattering has been greatly reduced. In addition, due to the proposed combination of the adaptive algorithm of back EMF gain and the back EMF observer, the problem of phase delay caused by LPF in the conventional SMO has been solved and the estimated accuracy of rotor position at low speed has been further enhanced. With this proposed sensorless control algorithm, the FMPM wheel motor could be operated from 5% to 100% rated speed with good tracking capability, fast dynamic, and strong robustness.

The evaluation of system performances has been implemented by simulation and experiment based on a prototype of the new FMPM wheel motor. Both the simulated and experimental results have demonstrated the feasibility and validity of this sensorless SVPWM-FADTC driving system for the new FMPM wheel motor. Furthermore, this paper has provided a certain reference value for the sensorless control scheme based on back EMF to widen the estimated range.

REFERENCES

[1] K. Atallah and D. Howe, "A novel high performance magnetic gear," *IEEE Trans. Magn.*, vol. 37, no. 4, pp. 2844–2846, Jul. 2001.

[2] L. Jian and K. T. Chau, "A coaxial magnetic gear with Halbach permanent-magnet arrays," *IEEE Trans. Energy Convers.*, vol. 25, no. 2, pp. 319–327, Jun. 2010.

[3] K. T. Chau, D. Zhang, J. Z. Jiang, C. Liu, and Y. Zhang, "Design of a magnetic-geared outer-rotor permanent-magnet brushless motor for electric vehicles," *IEEE Trans. Magn.*, vol. 43, no. 6, pp. 2504–2506, Jun. 2007.

[4] Y. C. Zhang, J. G. Zhu, Z. M. Zhao, W. Xu, and D. G. Dorrell, "An Improved Direct Torque Control for Three-Level Inverter-Fed Induction Motor Sensorless Drive," *IEEE Trans. Power Electron.*, vol. 27, no. 3, pp. 1502–1513, Mar. 2012.

[5] C. L. Xia, J. X. Zhao, Y. Yan, and T. N. Shi, "A novel direct torque control of matrix converter-fed PMSM drives using duty cycle control for torque ripple reduction," *IEEE Trans. Ind. Electron.*, vol. 61, no. 6, pp. 2700–2713, Jun. 2014.

[6] E. B. Bassem, B. Badii, and M. Ahmed, "Bus clamping-based DTC: An attempt to reduce harmonic distortion and switching losses," *IEEE Trans. Ind. Electron.*, vol. 60, no. 3, pp. 4069–4077, Mar. 2013.

[7] Z. F. Zhang, R. Y. Tang, B. D. Bai, and D. X. Xie, "Novel direct torque control based on space vector modulation with adaptive stator flux observer for induction motors," *IEEE Trans. Magn.*, vol. 46, no. 8, pp. 3133–3136, Aug. 2010.

[8] L. X. Tang, L. M. Zhong, M. F. Rahman, and Y. W. Hu, "A novel direct torque controlled interior permanent magnet synchronous machine drive with low ripple in flux and torque and fixed switching frequency," *IEEE Trans. Power Electron.*, vol. 19, no. 2, pp. 346–354, Mar. 2004.

[9] C. Tian, H. P. Li, and Y. W. Hu, "A novel scheme of direct torque control in the permanent magnet synchronous motor drive," *IEEE Trans. Power Electron.*, pp. 47–52, Mar. 2002.

[10] Q. H. Liu, A. M. Khambadkone, and A. Tripathi, "Torque control of IPMSM drives using direct flux control for wide speed operation," in *Proc. IEEE Int. Elect. Mach. Drives Conf.*, 2003, pp. 188–194.

[11] G. L. Wang, R. F. Yang, and D. G. Xu, "DSP-based control of sensorless IPMSM drives for wide-speed-range operation," *IEEE Trans. Ind. Electron.*, vol. 60, no. 2, pp. 720–727, Feb. 2013.

[12] X. Wang *et al.*, "Position Self-Sensing Evaluation of Novel CW-IPMSMs With an HF Injection Method," *IEEE Trans. Ind. Appl.*, vol. 50, no. 5, pp. 3325–3334, Sep./Oct. 2014.

[13] T. C. Lin, L. M. Gong, J. M. Liu, and Z. Q. Zhu, "Investigation of saliency in a switched-flux permanent-magnet machine using high-frequency signal injection," *IEEE Trans. Ind. Electron.*, vol. 61, no. 9, pp. 5094–5104, Sep. 2014.

[14] J. M. Liu and Z. Q. Zhu, "Improved Sensorless Control of Permanent-Magnet Synchronous Machine Based on Third-Harmonic Back EMF," *IEEE Trans. Ind. Appl.*, vol. 50, no. 3, pp. 1861–1870, May/Jun. 2014.

[15] Y. C. Shi, K. Sun, L. P. Huang, and Y. D. Li, "Online identification of permanent magnet flux based on extended Kalman filter for IPMSM drive with position sensorless control," *IEEE Trans. Ind. Electron.*, vol. 59, no. 11, pp. 4169–4178, Nov. 2012.

[16] M. Liu, L. x. Zhang, P. Shi, and H. R. Karimi, "Robust control of stochastic systems against bounded disturbances with application to flight control," *IEEE Trans. Ind. Electron.*, vol. 61, no. 3, pp. 1504–1515, Mar. 2014.

[17] L. Yuan *et al.*, "Sensorless control of high-power interior permanent magnet synchronous motor drives at very low speed," *IET Electr. Power Appl.*, vol. 7, no. 3, pp. 199–206, May 2013.

[18] J. B. Chu *et al.*, "An improved sliding mode observer for position sensorless vector control drive of PMSM," in *Proc. IEEE PEMC*, May 2009, pp. 1898–1902.

[19] Z. W. Qiao *et al.*, "New sliding-mode observer for position sensorless control of permanent-magnet synchronous motor," *IEEE Trans. Ind. Electron.*, vol. 60, no. 2, pp. 710–719, Feb. 2013.

[20] S. Chi, Z. Zhang, and L. Y Xu, "Sliding-mode sensorless control of direct-drive PM synchronous motors for washing machine applications," *IEEE Trans. Ind. Appl.*, vol. 45, no. 2, pp. 582–490, Mar./Apr. 2009.

[21] A. Toba and T. Lipo, "Generic torque-maximizing design methodology of surface permanent-magnet vernier machine," *IEEE Trans. Ind. Appl.*, vol. 36, no. 6, pp. 1539–1546, Nov./Dec. 2000.

[22] L. L. Wang, J. X. Shen, and H. Hao, "Development of a Magnetic-Geared Permanent-Magnet Brushless Motor," *IEEE Trans. Magn.*, vol. 45, no. 10, pp. 4578–4581, Oct. 2009.

[23] C. H. Liu, J. Zhong, and K. T. Chau, "A novel flux-controllable vernier permanent-magnet machine," *IEEE Trans. Magn.*, vol. 47, no. 10, pp. 4238–4241, Oct. 2011.

[24] Y. Fan, L. Zhang, and M. S. Wei, "The improved direct torque control of a new self-decelerating permanent-magnet in-wheel motor for electric vehicles," in *Proc. IEEE VPPC*, 2013, pp. 1–5.

[25] V. Utkin and H. C. Chang, "Sliding mode control on electro-mechanical system," *Math. Problem Eng.*, vol. 8, no. 4/5, pp. 451–473, 2002.

Ying Fan (M'07–SM'14) received the B.Sc. and M.Sc. degrees from Nanjing University of Astronautics and Aeronautics, Nanjing, China, in 1991 and 1996, respectively, and the Ph.D. degree in electrical and electronic engineering from The University of Hong Kong, Pokfulam, Hong Kong, in 2006.

Currently, she serves as an Associate Professor with and the Deputy Dean of the Department of Electric Machine and Control, Southeast University, Nanjing. Her teaching and research interests focus on electric drives, electric vehicles, and wind power generation. She has published more than 25 technical papers and holds 18 patents in these areas.

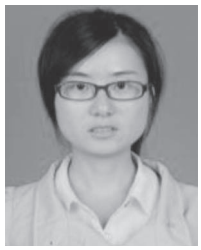

Li Zhang (S'13) received the B.S. degree in electrical engineering and automation in 2010 from Jiangsu University, Zhenjiang, China, and the M.S. degree in electrical engineering in 2013 from Southeast University, Nanjing, China, where she is currently working toward the Ph.D. degree.

Her research interests include motor design and motor drives.

Ming Cheng (M'01–SM'02–F'15) received the B.Sc. and M.Sc. degrees from Southeast University, Nanjing, China, in 1982 and 1987, respectively, and the Ph.D. degree from The University of Hong Kong, Pokfulam, Hong Kong, in 2001.

Since 1987, he has been with Southeast University, where he is currently a Professor with the School of Electrical Engineering and the Director of the Research Center for Wind Power Generation. He has authored or coauthored more than 300 technical papers and five books, and he holds more than 50 patents in these areas. His teaching and research interests include electrical machines, motor drives for electric vehicles, and renewable energy generation.

Prof. Cheng is a Fellow of The Institution of Engineering and Technology, U.K. He has served as the Chair and as an Organizing Committee Member for many international conferences.

K. T. Chau (M'89–SM'04–F'13) received the B.Sc.(Eng.), M.Phil., and Ph.D. degrees from The University of Hong Kong, Pokfulam, Hong Kong, in 1988, 1991, and 1993, respectively, all in electrical and electronic engineering.

Since 1995, he has been with The University of Hong Kong, where he is currently a Professor with the Department of Electrical and Electronic Engineering and the Director of the International Research Centre for Electric Vehicles. He is the author of four books and more than 400 refereed technical papers. His research interests include electric and hybrid vehicles, power electronics and drives, and renewable energy.

Prof. Chau is a Chartered Engineer in the U.K. He is a Fellow of The Institution of Engineering and Technology, U.K., and the Hong Kong Institution of Engineers. He currently serves as a Coeditor of the *Journal of Asian Electric Vehicles*. He was a recipient of the Changjiang Chair Professorship from the Ministry of Education, China, and the Environmental Excellence in Transportation Award for Education, Training, and Public Awareness from SAE International.